ACS Biomaterials SCIENCE & ENGINEERING

pubs.acs.org/journal/abseba

Article

Stable and Antibacterial Magnesium−Graphene Nanocomposite-Based Implants for Bone Repair

Narges Safari,[▽] Nasim Golafshan,[▽] Mahshid Kharaziha,* Mohammad Reza Toroghinejad, Lizette Utomo, Jos Malda, and Miguel Castilho*

Cite This: *ACS Biomater. Sci. Eng.* 2020, 6, 6253−6262

Read Online

ACCESS | Metrics & More | Article Recommendations | Supporting Information

ABSTRACT: Magnesium (Mg)-based alloys are promising biodegradable materials for bone repair applications. However, due to their rapid degradation and high corrosion rate, Mg-based alloys are typically associated with *in vivo* infections and implant failure. This study evaluated the synergistic stability and anti-inflammatory properties that could potentially be achieved by the modification of the Mg alloy with graphene nanoparticles (Gr). Incorporation of low dosages of Gr (0.18 and 0.50 wt %) in a Mg alloy with aluminum (Al, 1 wt %) and copper (Cu, 0.25 wt %) was successfully achieved by a spark plasma sintering (SPS) method. Notably, the degradation rate of the Mg-based alloys was reduced approximately 4-fold and the bactericidal activity was enhanced up to 5-fold with incorporation of only 0.18 wt % Gr to the Mg−1Al−Cu matrix. Moreover, the modified Mg-based nanocomposites with 0.18 wt % Gr demonstrated compressive properties within the range of native cancellous bone (modulus of approximately 6 GPa), whereas *in vitro* studies with human mesenchymal stromal cells (hMSCs) showed high cytocompatibility and superior osteogenic properties compared to non-Gr-modified Mg−1Al−Cu implants. Overall, this study provides foundations for the fabrication of stable, yet fully resorbable, Mg-based bone implants that could reduce implant-associated infections.

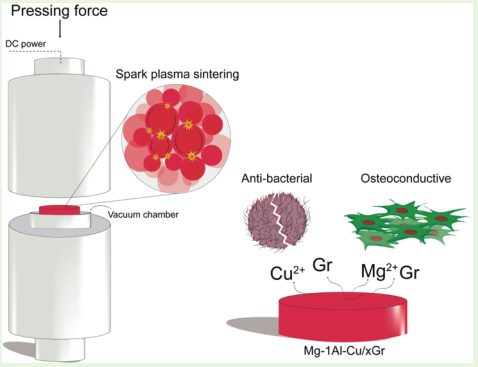

KEYWORDS: *magnesium alloys, degradation, corrosion resistance, antibacterial properties, bone implants*

1. INTRODUCTION

Despite intensive research over the last decade, shortage of bone implants with acceptable resorbability and load-bearing properties still remains a major problem in orthopedic and musculoskeletal surgery.[1−3] Metallic bone implants made of titanium,[4,5] stainless steel,[6] cobalt-chrome,[7] and magnesium (Mg)-based alloys[8] are still the only clinical available solutions to ensure stable and sustained support during *in vivo* service. Among these, magnesium-based metals are one of the most promising metallic biomaterials due to their *in vivo* resorbability and unique osteopromotive properties.[9,10] Mg-based alloys are known to be extremely active materials that can degrade in physiological conditions due to their electrochemical properties, in particular, due to their low standard electrode potential.[11] Unfortunately, such strong electronegativity leads to accelerated implant surface corrosion and formation of voids within the bulk material structure, which in most cases cause premature loss of implant mechanical integrity.[12]

To overcome the fast degradation rate of Mg-based implants, incorporation of low dosages of metal ions, like zinc, aluminum (Al), manganese, copper (Cu), and zirconium, within the Mg matrix has been explored.[13−15] In particular, researchers have recently shown that the combination of Mg with Al and Cu (Mg−1Al−Cu) could decrease the *in vitro* degradation of Mg-based implants while simultaneously introducing antibacterial properties.[16] Despite the promising properties of the Mg−1Al−Cu alloy, the reported degradation rate was still too fast to meet the bone growth rate and the ability to support sufficient bone formation was not demonstrated. In addition, eradication of the bacterial biofilm that formed on the implant surface remained a major risk, which requires further strategies to mitigate implant-associated infection.[17,18]

As an alternative to the conventionally used metal-ion additives, graphene (Gr)-based nanocomposites have been explored.[19,20] Gr is composed of carbon atoms arranged in a flat honeycomb structure and possesses unique mechanical strength[21] and antibacterial[22] and osteogenic properties.[23] However, a recent study reported the enhanced corrosion resistance of Mg-based implants when combined with graphene oxide (GO).[19] We here hypothesize that the incorporation of Gr within the Mg−1Al−Cu alloy will

Received: April 24, 2020
Accepted: September 25, 2020
Published: September 25, 2020

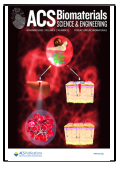

https://dx.doi.org/10.1021/acsbiomaterials.0c00613
ACS Biomater. Sci. Eng. 2020, 6, 6253−6262

reduce/inhibit/slow down the degradation of Mg−1Al−Cu implants while simultaneously providing antibacterial and osteopromotive properties. To incorporate the Gr within the Mg−1Al−Cu matrix, a spark plasma sintering (SPS) method was used, and different amounts of Gr nanoparticles (0.18 and 0.5 wt %) were investigated. After fabrication, the degradation rate, mechanical properties, antibacterial activity, and cytocompatibility of the prepared Mg-based implants were thoroughly investigated and compared with non-Gr-modified Mg−1Al−Cu implants. In addition, the osteogenic potential of the generated materials was evaluated *in vitro* over 14 days under culture conditions with and without osteoinductive agents.

2. MATERIALS AND METHODS

2.1. Materials and Processing. Magnesium (purity 99.8%, particle size <70 μm), aluminum (purity 99.8%, particle size <60 μm), and copper (purity 99.8%, particle size <63 μm) powders and stearic acid were purchased from Merck Company, Germany. Graphene nanoparticles (purity 99.5%, particle size <100 nm, <32 layers) were obtained from Nanosany Corporation, Iran.

Mg−1Al−Cu/*x*Gr nanocomposites were prepared using a two-step process that included milling and SPS. At first, to synthesize the intermetallic phase (Al_2Cu), Al and Cu powders in a weight ratio of 80:20 were mixed in a high-energy ball-mill (Retsch Pm100 model, Germany) at 200 rpm for 20 h (1Al−Cu). To prevent powder agglomeration, 1 wt % stearic acid was added prior to the milling process. Then, two different concentrations of Gr (0.18 and 0.5 wt %) were added to the Al_2Cu mixture and mechanically ball-milled for at least 4 h (1Al−Cu/*x*Gr). To prepare the powder for SPS, Mg−1Al−Cu/*x*Gr suspensions were made by dispersing the 1Al−Cu/0.18Gr and 1Al−Cu/0.5Gr in Mg powders with weight ratios of 3:197 and 4:196, respectively. The Mg−1Al−Cu/*x*Gr suspensions were mixed using a mechanical agitator with the speed of 2000 rpm for 3 h and dried in a vacuum oven (Teb Azma, Iran) at 70 °C for 2 h. After milling, the nanocomposite powders were compacted into a Gr mold (Ø = 15 mm) and then sintered using an in-house-modified spark plasma device (SPS, KPF Model, Iran). The sintering process was conducted for 10 min at a heating rate of 75 °C/min, constant temperature of 600 °C, and pressure of 40 MPa. 1Al−Cu/0.18Gr, 1Al−Cu/0.5Gr, and Mg−1Al−Cu without Gr were also prepared as control groups following a similar protocol.

2.2. Physical and Chemical Characterization. X-ray diffraction (XRD) analysis was performed after each step of the fabrication process using Cu Kα radiation (λ = 0.154 nm) at 40 kV and 40 mA (XRD, Phillips, Germany). XRD patterns were collected with 2θ ranging from 20 to 70° and a scan step size of 0.05°. The microstructure of Mg−1Al−Cu/*x*Gr nanocomposites was analyzed using a scanning electron microscope (SEM, Philips, XL30, Germany) equipped with an electron backscatter diffraction (EBSD) detector and X-ray mapping (Oxford EDX system, U.K.). Prior to imaging, all samples were coated with a 6 nm gold layer. In addition, the density of Mg−1Al−Cu/*x*Gr nanocomposites was determined by the Archimedes principle, according to a protocol described elsewhere.[24] Theoretical densities were calculated by the rule of mixture, assuming theoretical densities of each individual material of ρ_{Mg} = 1.73 g/cm^3, ρ_{Al} = 2.7 g/cm^3, and ρ_{Cu} = 8.96 g/cm^3.[25−27]

2.3. Mechanical Characterization. Uniaxial compression testing was carried on a Hounsfield H25KS universal testing machine equipped with a 1 kN load cell, at room temperature. Compression tests were performed on dense samples with 3 mm × 3 mm × 6 mm size (n = 3), at a rate of 0.5 mm/min, according to the ASTM E9-89a (2000) standard.[28] From the engineered stress−strain curves, compressive strength, compressive modulus, and strain at breakpoint were calculated. The compressive strength was determined as the maximum compressive stress until the sample breakpoint. The compressive modulus was defined as the slope of the linear region of the stress−strain curves from 0.02 to 0.05 mm/mm strain. After compression, the fractured surface of the tested samples was evaluated by SEM analysis.

2.4. Degradation Rate Evaluation. The degradation rate of Mg−1Al−Cu/*x*Gr samples (8 mm × 6 mm × 2 mm) was investigated in simulated body fluid (SBF) solution at 37 °C and pH of 7.4 for 10 h, following the ASTM-G31-72 standard.[29] Degradation rate, weight loss, and hydrogen release rate were examined every 2 h during the immersion period in SBF (n = 3). To evaluate implant degradation, the rate of hydrogen released was measured during the corrosion process, according to a method described in detail elsewhere.[16] Briefly, the released hydrogen bubbles were collected in a funnel, and the change in SBF volume was quantified in a graded buret connected to the funnel. Corrosion products formed during degradation were evaluated by XRD, SEM, and energy-dispersive X-ray (EDX) techniques. In addition, the weight loss (W_{loss}) of samples was determined as

$$W_{loss} = \frac{W_1 - W_2}{W_2} \times 100 \quad (1)$$

where W_1 and W_2 are the sample weights before and after immersion, respectively. The degradation rate was quantified as

$$\text{degradation rate}(\text{mm h}^{-1}) = \frac{W}{A \times T \times \rho} \quad (2)$$

where A is the sample area (mm^2), T is the immersion time (h), and ρ is the theoretical density of the samples (g/mm^3).

2.5. *In Vitro* Antibacterial Assay. Antimicrobial activity of the Mg−1Al−Cu/*x*Gr was evaluated by the extraction of implants in phosphate-buffered saline (PBS) at the concentration of 12 mg/mL according to the methods described in a previous study.[16] The antimicrobial activity of the extracts was tested against *Staphylococcus aureus* (ATCC 25923) and *Escherichia coli* (ATCC 25922) bacteria (Ideal Gostar co, Iran), and was evaluated using a disk-diffusion agar method, as described elsewhere.[30] Tests were performed in sterile Petri dishes (Ø = 5 cm) containing brain heart infusion (BHI) agar medium and the extracts of the nanocomposite powders (12 mg/mL). The agar plates were prepared and coated with the bacteria at a concentration of 5 × 10^6 per colony-forming unit (CFU)/mL. Sample extracts were incubated at 37 °C for 24 h. The antibacterial behavior of the Mg−1Al−Cu/*x*Gr nanocomposites was determined according to the disc-diffusion method by quantifying the bacteria inhibition zone. In addition, the bacteria morphology was investigated by SEM analysis. Before imaging, both *S. aureus* and *E. coli* bacteria were incubated in fresh media at 37 °C for 24 h. Next, the Mg−Al−Cu/*x*Gr extracts (12 mg/mL) were added to the solution containing the bacteria (5 × 10^6 CFU/mL) and incubated in an orbital shaker (150 rpm) at 37 °C for 24 h. After treatment, samples were centrifuged at 4000 rpm for 10 min, and bacteria were washed with PBS and then fixed in 2.5% glutaraldehyde (Sigma-Aldrich, Germany) for 2 h and dehydrated in a series of ethanol solutions. After dehydration, 10 μL of each sample was placed on a glass slide and dried on air for 24 h. Finally, the samples were gold-coated and imaged by SEM (Philips, XL30, Germany), at an acceleration voltage of 20 kV.

Generation of reactive oxygen species (ROS) was investigated using the ROS assay kit (Teb Pazhouhan Razi, Iran) according to the manufacturer's protocol and determined using dichlorofluorescein diacetate (DCFH-DA, Merck, Germany) as a fluorescent probe. Briefly, after incubation of *S. aureus* and *E. coli* bacteria in broth media, the extractions of Mg−1Al−Cu/*x*Gr implants (12 mg/mL) were added to the bacteria suspension at the concentration of 5 × 10^6 CFU/mL, and they were shaken at 150 rpm in an orbital shaker at 37 °C for 24 h. Consequently, the media was removed by centrifuging the bacteria suspension at 1200 rpm for 2 min, which was then washed with PBS, treated with 100 μL of DCFH-DA and incubated at 37 °C for 1 h in a dark room. Finally, bacterial pellets were centrifuged and washed to remove the DCFH-DA. As a positive control, samples treated with 100 μL of H_2O_2, and as a negative control, nontreated bacteria labeled with DCFH-DA, were also included. The intensity of fluorescence was measured with a

https://dx.doi.org/10.1021/acsbiomaterials.0c00613
ACS Biomater. Sci. Eng. 2020, 6, 6253−6262

Table 1. List of Primers Used

gene	accession no.	primer forward	primer reverse	product size	refs
GAPDH	NM_001289745	ATGGGGAAGGTGAAGGTCG	TAAAAGCAGCCCTGGTGACC	70	33
B2M	NM_004048	TGCTCGCGCTACTCTCTCTTT	TCTGCTGGATGACGTGAGTAAAC	82	33
RUNX2	NM_00102463	TTACAGTAGATGGACCTCGGGA	AGGAATGCGCCCTAAATCACT	104	N/A
COL1A1	NM_000088	AAGAGGAAGGCCAAGTCGAG	GTTTCCACACGTCTCGGTCA	96	34
SPP1	NM_000582	GCCGAGGTGATAGTGTGGTT	GTGGGTTTCAGCACTCTGGT	242	35

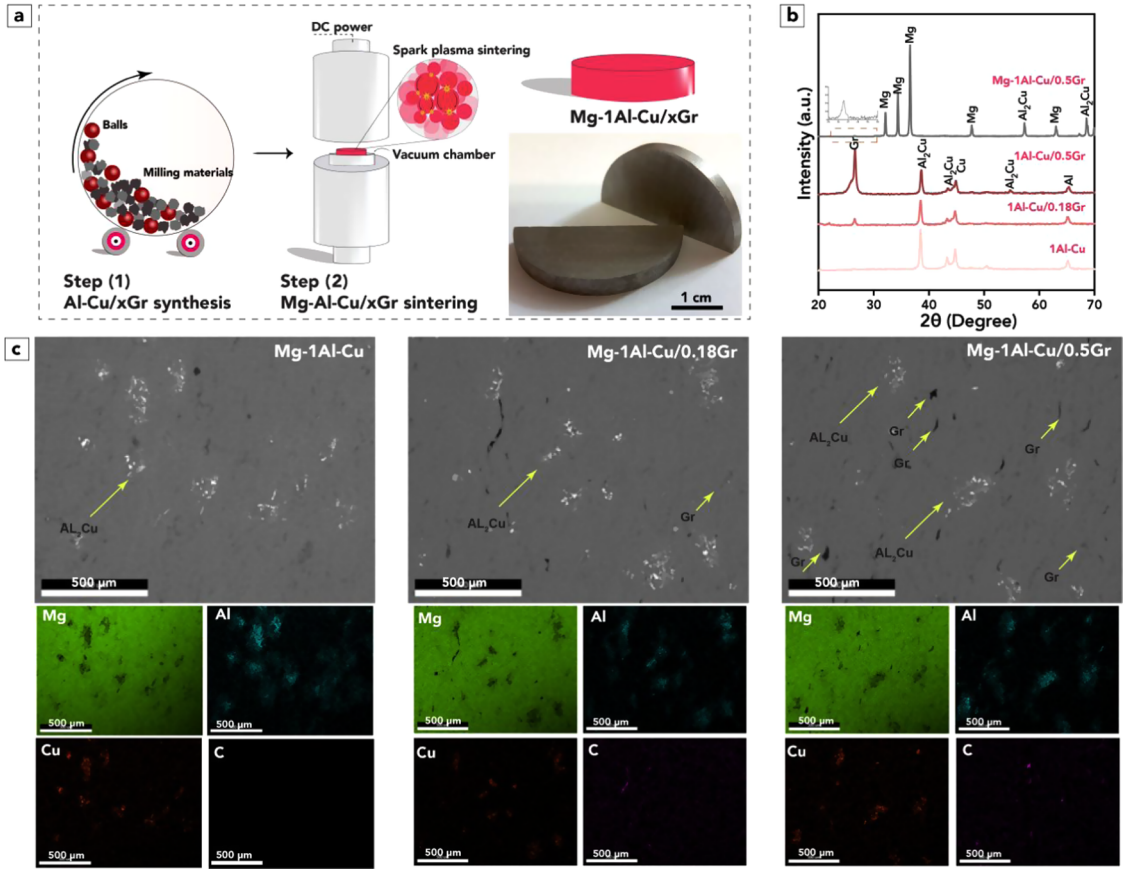

Figure 1. Fabrication and chemical properties of Mg−1Al−Cu/*x*Gr (*x* = 0, 0.18, and 0.5 wt %) nanocomposite samples. (a) Schematic of the two-step fabrication process, (b) XRD patterns of the 1Al−Cu, 1Al−Cu/*x*Gr, and Mg−1Al−Cu/*x*Gr samples after each processing step followed by (c) backscattered SEM micrographs and EDX-mapping analysis.

microplate reader (Biotek Instruments, China) at a wavelength of 490 nm.

2.6. *In Vitro* Cytocompatibility and Osteogenic Potential Evaluation. Human mesenchymal stromal cells (hMSCs, passage number 3) were derived from healthy human donors after obtaining informed consent approved by the Biobank Research Ethics Committee (University Medical Center Utrecht). hMSCs were cultured in α-MEM (Gibco) supplemented with 10% (v/v) fetal bovine serum (FBS, Gibco, USA), 1% (v/v) ascorbic acid (Gibco), and 1% (v/v) penicillin/streptomycin (Gibco) at 37 °C in a humidified atmosphere containing 5% CO_2. In this regard, hMSCs with a density of 800 cells/well were seeded in the 48-well plates and after 24 h of incubation, the culture medium was replaced with the extracted suspension in basal media. After 24 h, the cells were in direct contact with the extracts of Mg−1Al−Cu/*x*Gr (*x* = 0, 0.18, and 0.5 wt %) powders with the concentration of 12 mg/mL (conditioned medium), based on a concentration optimized elsewhere.[16]

On day 7, half of the samples were changed to an osteogenic media (α-MEM + 10% FBS + 0.2 mM ASAP + 1% Pen−Strep + 10 nM dexamethasone + 10 mM B-glycerophosphate, Sigma-Aldrich, Germany), while the other half was kept in basal media for 14 days. On days 1, 7, and 14 of culture, the metabolic activity of the different extracts was evaluated with the Alamar blue assay, by incubating the cell-seeded samples with a 10 wt % Alamar blue reagent (Thermo Scientific) in a culture medium for 2 h. The fluorescence at 590/620 nm was detected using a Fluroskan Ascent plate reader (Labsystems, Helsinki, Finland).

Cell morphology was investigated using the immunostaining assay (actin staining). Samples were fixed with 4% (v/v) paraformaldehyde (Sigma-Aldrich, Germany) for 30 min and then permeated in 0.2% (v/v) Triton for 10 min. Subsequently, samples were incubated with Rhodamine Phalloidin (Alexa flour 488, Abcam, U.K.) at 1:40 dilution and 6-diamidino-2-phenyl indole dihydrochloride (DAPI, Abcam, U.K.) at a 1:1000 dilution to stain cytoskeletal organization of actin filaments (red color) and cell nuclei (blue color), respectively. Then, samples were imaged by a fluorescence microscope (IX5, Olympus, Tokyo, Japan), and the fluorescence signals from phalloidin-TRITC and DAPI were collected at Ex/Em 493/517 and 500 nm, respectively. The cell cytoskeleton area was calculated using Image J software.

Early osteogenic differentiation of hMSCs was evaluated using the alkaline phosphatase (ALP) assay after 4, 7, and 14 days of culture. The intracellular ALP activity of hMSCs was investigated by BCIP/NBT (5-bromo-4-chloro-3-indolyl phosphate/Nitro blue tetrazolium,

https://dx.doi.org/10.1021/acsbiomaterials.0c00613
ACS Biomater. Sci. Eng. 2020, 6, 6253−6262

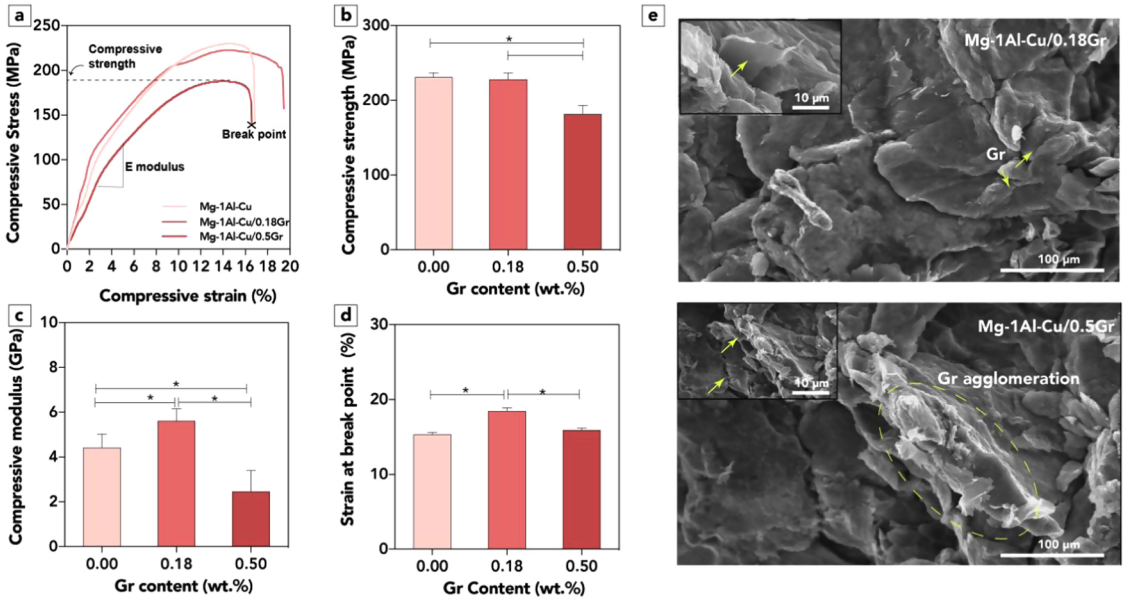

Figure 2. Compressive properties of Mg−1Al−Cu/xGr (x = 0, 0.18, and 0.5) nanocomposite samples. (a) Representative compressive stress−strain curves and determined (b) ultimate strength, (c) compressive modulus, and (d) strain at break, as a function of the Gr content (*P < 0.05). (e) Representative SEM images of fractured sample sections after compression testing.

Thermo Scientific) solution, after DPBS washing steps. Afterward, the samples were incubated in a light-protective environment for 2 h at room temperature, washed with PBS, and imaged by a Leica DMi1 microscope (Carl Zeiss, Germany). The ALP-stained area was determined by Image J software. To evaluate the osteogenic differentiation capacity of the materials, hMSCs (n = 1 donor in triplicate, passage number = 3) were seeded at a density of 2600 cells/cm^2 in 12-well plates in a basal medium (α-MEM supplemented with 10% (v/v) fetal bovine serum, 1% (v/v) ascorbic acid, and 1% (v/v) penicillin/streptomycin). The extracts of the samples were supplemented at 12 mg/mL to the basal or osteogenic medium. As controls, cells were plated in monolayers without the materials and differentiated with an osteogenic medium for 7 and 14 days. To evaluate gene expression, the cells were lysed using the TRIzol reagent (Thermofisher Scientific) and 20% chloroform (Sigma-Aldrich, Germany). mRNA was extracted from the aqueous phase and was quantified using a NanoDrop ND1000 spectrophotometer (Thermo Fisher Scientific) at 260/280 nm. cDNA was synthesized using the iScript cDNA Synthesis Kit (Bio-Rad) according to the manufacturer's instructions. PCR analyses of Runt-related transcription factor 2 (*RUNX2*), collagen type I (*COL1A1*), and osteopontin (*SPP1*) were done with a Bio-Rad CFX96 Real-Time PCR Detection System (Bio-Rad) using FastStart SYBR Green Master mix (Sigma-Aldrich, Germany). Glyceraldehyde-3-phosphate dehydrogenase (*GAPDH*) and β-2-microglobulin (*B2M*) were used to determine a best-housekeeping index (BHKi),[31] which was used as reference for the expression of the genes of interest. The relative expression was determined by the $2^{-\Delta C_T}$ method. C_T-values above 40 were considered undetectable. Primers used are listed in Table 1, and all primers have an efficiency between 0.90 and 1.00. The primers used were designed and validated as described elsewhere.[32]

2.7. Statistical Analysis. Statistical analysis was performed by GraphPad Prism software (V.6). All experiments were performed at least three times and reported as the mean ± standard deviation (SD). The significant difference between groups was determined *via* the one-way analysis of variance (ANOVA) with Tukey's post hoc test. Differences were considered significant at a probability error (p) of p < 0.05.

3. RESULTS AND DISCUSSION

3.1. Implant Composition and Microstructure Analysis. Mg−1Al−Cu/xGr nanocomposites were successfully manufactured using a two-step fabrication process that involved ball-milling followed by SPS, as illustrated in Figure 1a. XRD analysis confirmed that the intermetallic phase of Al_2Cu was formed after 20 h of milling and that Gr was successfully incorporated within the Mg−1Al−Cu matrix after SPS (Figure 1b). As expected, the Gr peak (2θ = 26.5°) was more pronounced for the 0.5 wt % Gr implants as for 0.18 wt % Gr implants, which indicates a higher final amount of Gr in the 0.5 wt % Gr implants.

From the backscattered SEM micrographs, it was observed that both Gr (black-color deposits) and Al_2Cu (white-color phase) were homogenously dispersed within the Mg−1Al−Cu matrix material (Figure 1c). However, with the increase of Gr concentration from 0.18 to 0.5 wt %, an agglomeration of Gr nanoparticles, was noticed. The increase in Gr content and consequent Gr agglomeration resulted in a decrease in material density from 98.9 ± 0.3 to 96.3 ± 0.3% for Mg−1Al−Cu/0.5Gr and Mg−1Al−Cu/0.18Gr implants, respectively (Supporting Information Table S1). Similar agglomeration of Gr nanoparticles and consequent decrease in material density has also been observed by Yazdani and co-workers for Gr−Al_2O_3 nanocomposites,[36] although this was only noted for Gr concentrations above 0.5 wt %. This Gr agglomeration was attributed to the high energy absorption of individual Gr nanoparticles, which was shown to result in high attraction forces between particles.[37]

3.2. Mechanical Properties and Fracture Analysis. The effect of Gr addition on the mechanical performance of Mg-based implants was analyzed under uniaxial compression tests (Figure 2a). Although the addition of Gr resulted in a decrease in compressive strength (in particular for 0.5 wt % Gr implants), a 1.5-fold increase in compressive modulus and a 1.2-fold increase in failure strain were found for the 0.18 wt % Gr implants (Figure 2b−d). This increase is attributed to the more homogeneous dispersion of Gr within the Mg−1Al−Cu matrix, which acted as a cohesive element of Mg grains during sintering.[38] To investigate this further, the fractured surfaces of tested materials were investigated by scanning electron

https://dx.doi.org/10.1021/acsbiomaterials.0c00613
ACS Biomater. Sci. Eng. 2020, 6, 6253−6262

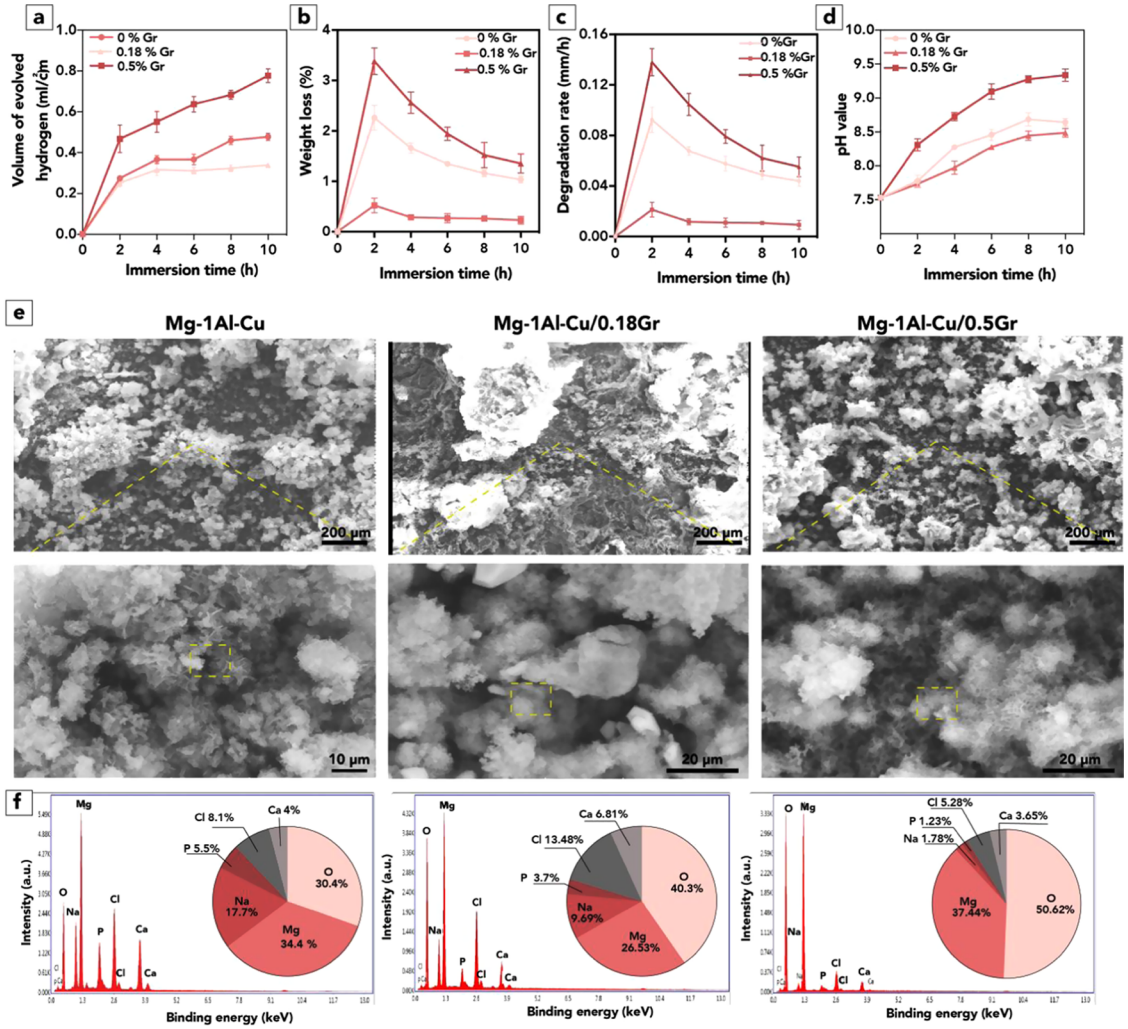

Figure 3. Degradation behavior of Mg−1Al−Cu/*x*Gr nanocomposite (*x* = 0, 0.18, and 0.5 wt %) samples in SBF solution over 10 h. (a) Volume of hydrogen released and respective samples' (b) weight loss and (c) degradation rate *D*. pH evaluation of the SBF soaking solution. Representative (d) SEM images and (e) EDX elemental composition of corroded surfaces (dashed square box).

microscopy (Figure 2e). While a uniform distribution of Gr was confirmed for the Mg−1Al−Cu/0.18Gr samples, large and heterogeneously distributed Gr agglomerates (with a length of 111 ± 16 μm) were observed in the Mg−1Al−Cu/0.5Gr samples. Such large agglomerates formed inner flaws within the Mg-based matrix, which likely may have caused the mechanical weakening of Mg−1Al−Cu/0.5Gr samples. Similar findings were reported by Das and co-authors for other Mg-based alloys blended with GO particles in concentrations above 0.8−1 wt %.[39] Notably, the final compressive modulus of the Mg−1Al−Cu/*x*Gr implants was within the range of the values reported for human cancellous bone (3−20 GPa),[10] which confirms the suitability of this composite as a load-bearing material.

3.3. Degradation Behavior. To investigate the degradation of Mg−1Al−Cu/*x*Gr, implants were soaked in an SBF solution for 10 h, and hydrogen gas (H_2) release as well as implant weight was measured every 2 h (Figure 3). As previously shown, the degradation of Mg-based implants in an aqueous medium is accompanied by H_2 release and consequent formation of a $Mg(OH)_2$ film at the surface of the implants according to the chemical reaction

$$Mg_{(s)} + 2H_2O_{(aq)} \rightarrow Mg(OH)_{2(s)} + H_{2(g)} \quad (3)$$

Here, we show that the addition of 0.18 wt % Gr to the Mg−1Al−Cu matrix significantly decreases H_2 gas release from 0.38 ± 0.07 to 0.25 ± 0.03 mL/cm^2 (Figure 3a). Evaluation of weight loss, and the respective degradation rate, revealed an almost 4-fold decrease for Mg−1Al−Cu/0.18Gr samples (Figure 3b,c). The enhanced degradation rate in the presence of the Gr nanoparticles is attributed to the formation of passivation layers, which have prevented electrons from reaching, and therefore completing, the reduction of hydrogen ions to form hydrogen gas ($2H^+ + 2e^- \rightarrow H_2$).[40−42] This mechanism slowed down significantly the corrosion rate of Mg−1Al−Cu/0.18Gr implants. Interestingly, in the samples containing 0.5 wt % Gr. (Mg−1Al−Cu/0.5Gr), a significant increase in weight loss (1.2-fold) and the respective degradation rate (1.1-fold) was observed (Figure 3b,c). This is likely due to the agglomeration of Gr nanosheets in metal matrices, which stimulates the degradation due to the formation of galvanic corrosion.

To confirm the release of degradation products, the pH of the SBF solution was also monitored during the degradation tests (Figure 3d). A gradual increase in pH was observed for all of the investigated material compositions. This alkaline elevation of the SBF solution can be attributed to the release

https://dx.doi.org/10.1021/acsbiomaterials.0c00613
ACS Biomater. Sci. Eng. 2020, 6, 6253−6262

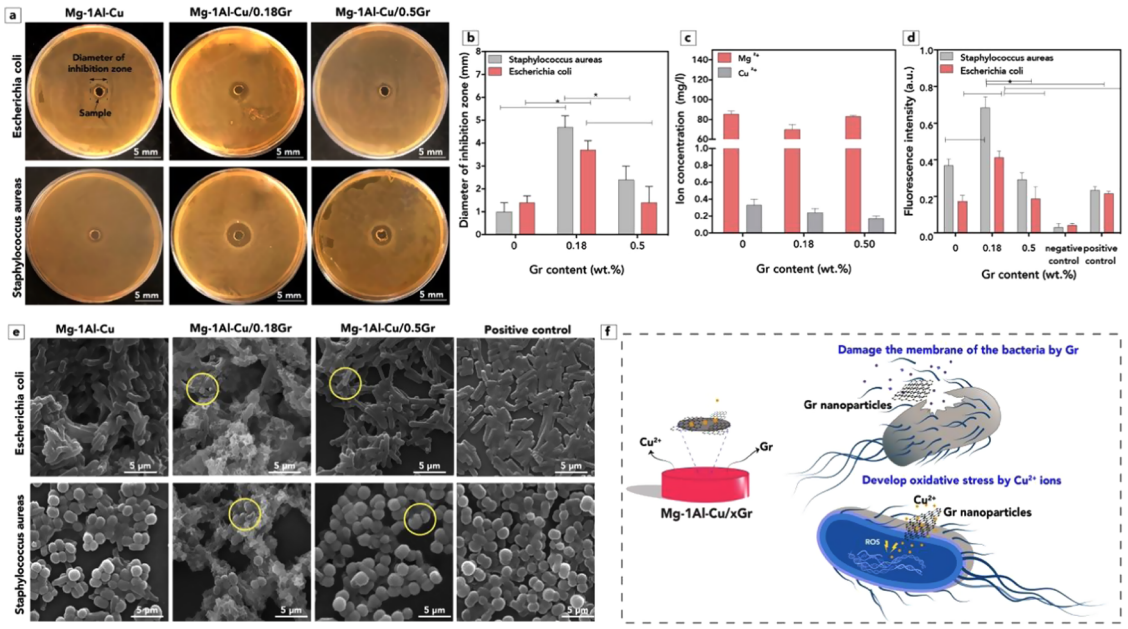

Figure 4. *In vitro* antimicrobial activity of Mg−1Al−Cu/*x*Gr nanocomposite (*x* = 0, 0.18, and 0.5 wt %) samples against *E. coli* and *S. aureus* bacteria after 24 h of incubation. (a) Stereoscopic images of the inhibition zone. (b) Comparison of the inhibition zone diameter (**P* < 0.05). (c) Ion release studies in Milli-Q water. (d) Relative fluorescence intensity showing reactive oxygen species (ROS) generation (**P* < 0.05). (e) Representative microscopic SEM images of bacteria morphology. (f) Schematic representation of predominant antibacterial mechanisms.

of OH^- ions and $Mg(OH)_2$ deposition at the implant surface. In accordance, a lower fluctuation of the pH value was observed for 0.18 wt % Gr composites (7.5−8.5) than for the 0.5 wt % Gr composites and non-Gr-modified Mg−1Al−Cu samples, which corroborates the H_2 release measurements.

To better understand the surface morphology and released degradation products, SEM and EDX analyses were performed (Figure 3e,f). In general, the 0.18 wt % Gr Mg−1Al−Cu samples showed a less corroded surface, with lower porosity and less apparent cracks, while the 0.5 wt % Gr and non-Gr-modified Mg−1Al−Cu samples presented a more corroded surface, with high porosity and with cauliflower- and needle-shaped corrosion products (Figure 3e). The EDX analysis confirmed a higher percentage of corrosion products (1.3- and 1.1-fold higher Mg and O elements, respectively) for 0.5 wt % Gr composites and nonmodified Mg composites than for 0.18 wt % Gr Mg−1Al−Cu implants. This difference could be ascribed to the formation of a $Mg(OH)_2$ film at the surface of the implant, as confirmed by XRD (Supporting Information, Figure S1). Interestingly, residues of precipitated hydroxyapatite (HA) were also observed at the implant surface. This could be attributed to the alkalinization of the SBF medium and the presence of calcium and phosphorus ions in the medium. Other studies also observed the formation of $Mg(OH)_2$ and HA in different Mg-based alloys (*e.g.*, calcium−magnesium−zinc, $Ca_{65}Mg_{15}Zn_{20}$) over 60 h of immersion in PBS solution.[43,44]

3.4. *In Vitro* Antibacterial Behavior. The antibacterial activity of Mg−1Al−Cu/*x*Gr implants was investigated against two kinds of bacteria, *S. aureus* and *E. coli*. Addition of Gr was observed to enhance antibacterial properties of Mg−1Al−Cu significantly (Figure 4). In particular, the 0.18 wt % Gr samples increased the diameter of the inhibition zone approximately 5- and 3-fold against *S. aureus* and *E. coli*, respectively, while the 0.5 wt % Gr samples increased the diameter of the inhibition zone approximately 3- and 1.1-fold against *S. aureus* and *E. coli*, respectively, when compared to non-Gr-modified Mg−1Al−Cu samples (Figure 4a,b). In addition, the release of Cu ions was observed to not change significantly (between 0.031 and 0.072 mg/L) as a function of the investigated Gr contents (Figure 4c). This observation reveals that the release of Cu ions alone cannot explain the improved antibacterial effect of the 0.18 wt % Gr implants. To investigate the mechanism of the antibacterial activity of Mg−1Al−Cu/*x*Gr implants further, additional analyses on ROS production and bacteria morphology were performed. ROS generation was monitored in *E. coli* and *S. aureus via* a fluorescent probe DCFH-DA (Figure 4d). Notably, ROS formations for Mg−1Al−Cu/0.18Gr were approximately 10 and 23 times higher than the negative controls for *E. coli* and *S. aureus* bacteria, respectively ($p < 0.05$). This revealed a high Gr-concentration-dependent effect on ROS formation, which is in accordance with previous work.[45] SEM analysis showed that Gr-modified implants, in particular the Mg−1Al−Cu/0.18Gr implants, induced a significant morphological change on both *E. coli* and *S. aureus* (Figure 4e). At a 0.18Gr concentration, dramatic cell lysis with extensive cellular debris was detected (yellow circles). Based on both analyses, the antibacterial mechanism of Mg−1Al−Cu/*x*Gr can be attributed to both the physical damage of the bacteria membranes by the sharp edges of Gr nanoparticles and to the formation of reactive oxygen species (ROS) (Figure 4f). These findings are in line with previous reports.[46−48] For example, Kiani and colleagues[49] attributed the antibacterial effect of graphene oxide (GO)-coated copper oxide nanowires to the sharp edges of GO, while Akhavan and colleagues[47] corroborated these findings by showing that the strong interaction between the sharp edges of Gr nanosheets and the *E. coli* and *S. aureus* damaged the cell membrane of the bacteria. Rajapaksha et al.,[45] on the other hand, attributed the antibacterial activity of copper-modified GO nanoparticles to the formation of reactive oxide species produced from the

https://dx.doi.org/10.1021/acsbiomaterials.0c00613
ACS Biomater. Sci. Eng. 2020, 6, 6253−6262

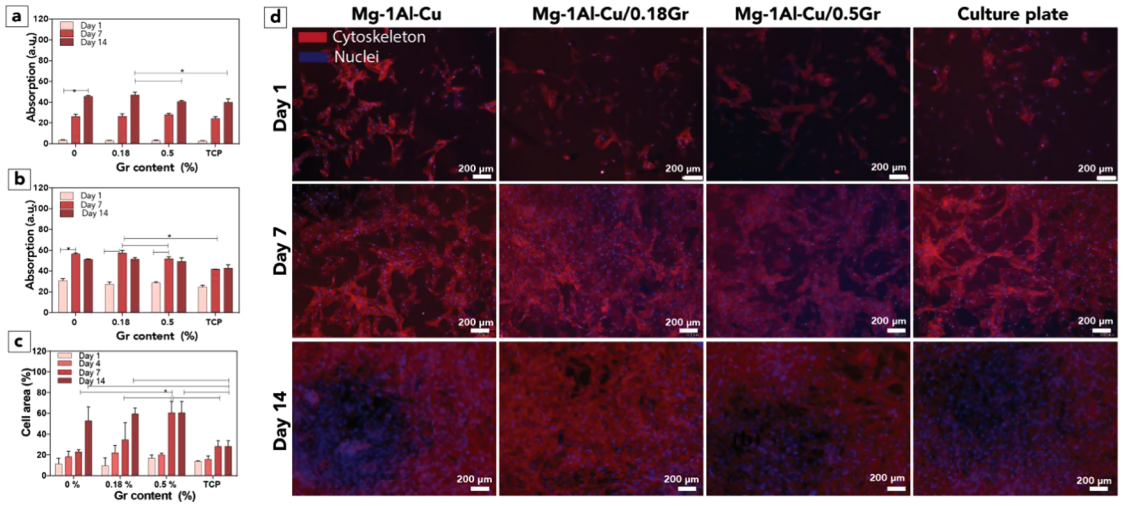

Figure 5. Cytocompatibility of the Mg−1Al−Cu/*x*Gr samples (x = 0, 0.18, and 0.5 wt %) over 14 days of *in vitro* culture with human mesenchymal stromal cells (hMSCs). Alamar blue quantification in (a) basal and (b) osteogenic media. (c) Cell area quantification (*P < 0.05). Non-Gr-modified Mg−1Al−Cu samples and culture plate were included as control groups. (d) Phalloidin (actin)/DAPI (nuclei) staining of hMSC proliferation on the sample surface.

copper oxide elements (*i.e.*, OH^-, O_2^-) that induce damage of the cell bacteria membrane.

3.5. *In Vitro* Cell Viability, Proliferation, and Osteogenic Potential. Cytocompatibility of Gr-modified Mg−1Al−Cu samples was confirmed with the quantitative Alamar blue assay, showing a steady increase in the total metabolic activity over 14 days, independent of the culture medium used, *i.e.*, basal or osteogenic (Figure 5a−c). In addition, release profile studies revealed maximum quantities of Cu (0.17−0.33 mg/L) and Mg (70−83 mg/L) ions within the recommended daily intake, *i.e.*, 10 mg/day for Cu and 420 mg/day for Mg ions[50−52] (Figure 4c). Furthermore, the addition of 0.18Gr to the Mg−1Al−Cu matrix was observed to prevent a burst release of Mg ions, which relates well with degradation results presented above. Previous reports on using coating strategies to combine GO particles with Mg-based samples were found to predominantly deposit GO particles at the sample's surface, which might generate cytotoxic conditions created by GO burst release.[53] This highlights well the advantages of the fabrication process here presented.

Furthermore, hMSCs were observed to more uniformly adhere and proliferate in the presence of Gr-modified materials than on non-Gr-modified Mg−1Al−Cu samples, when cultured in both basal (Figure 5d) and osteogenic (not shown) media. When comparing the cell area of proliferated cells, a 1.6- and a 1.8-fold increase were observed for Mg−1Al−Cu/0.18Gr samples in comparison to non-Gr-modified Mg−1Al−Cu samples and the culture plate, respectively. This further underscores the cytocompatibility of the Gr-modified Mg-based samples and could be, at least in part, explained by the lower degradation and consequent less alkaline surface environment of the Mg−1Al−Cu/0.18Gr samples, as compared to the non-Gr-modified Mg−1Al−Cu samples.

Addition of Gr to the Mg-based samples was also found to improve its osteogenic potential. After 7 and 14 days of *in vitro* culture, the alkaline phosphatase activity (ALP) for Mg−1Al−Cu/0.18Gr implants enhanced approximately 3.4-fold in the basal medium (Figure 6a,b) and 1.8-fold in the osteogenic medium (Figure 6b) when compared to the non-Gr-modified Mg−1Al−Cu samples. This enhancement might be explained by the noncovalent binding of proteins and osteogenic inducers to the Gr nanoparticles.[54] Similar observations were previously made by Yan et al., who described the enhancement of the ALP activity of rat MSCs after 7 days of culture on Gr-based nanotubes.[55] Above 0.5 wt % concentration, the osteogenic effect of Mg−1Al−Cu samples was, however, less evident. This was likely due to the faster degradation and alkalinization of the surface, preventing hMSC adhesion and potentially induced cell membrane disruption due to oxidative damage.[56,57] However, to clarify this, longer-term *in vitro* studies are clearly needed. Gene expression analysis confirmed that hMSCs in contact with Mg−1Al−Cu/*x*Gr in the osteogenic medium had similar expression levels of *RUNX2*, *COL1A1*, and *SPP1* than of the controls after 7 days of culture. This indicates that the materials supported, but did not synergistically enhance, osteogenic differentiation of hMSCs in monolayers. Interestingly, when the hMSCs were in contact with the materials and cultured in a basal medium for 14 days, expression levels were not detectable in the positive controls but still expressed, albeit low, by the hMSCs in contact with Mg−1A1−Cu/*x*Gr. These data indicate that contact of the metallic ions and Gr nanoparticles with hMSCs on its own can support osteogenic differentiation of hMSCs (Figure 6 e,f).

4. CONCLUSIONS

In conclusion, our results presented a novel and simple fabrication method for fully degradable, yet mechanically competent, Gr-modified Mg−1Al−Cu materials. Addition of only 0.18 wt % Gr nanoparticles to the Mg−1Al−Cu matrix notably decreases *in vitro* corrosion of Mg−1Al−Cu samples while simultaneously improving its antibacterial properties against two kinds of bacteria, *S. aureus* and *E. coli*. In addition, we demonstrated that the Gr-modified Mg−1Al−Cu samples are cytocompatible and that the 0.18 wt % Gr-modified Mg−1Al−Cu presented better cell proliferation and osteopromotive properties in terms of the osteogenic gene expression level than non-Gr-modified samples. Further studies will focus on extending the *in vitro* studies and characterization to better understand the benefits of Gr nanoparticles on bone tissue formation.

https://dx.doi.org/10.1021/acsbiomaterials.0c00613
ACS Biomater. Sci. Eng. 2020, 6, 6253−6262

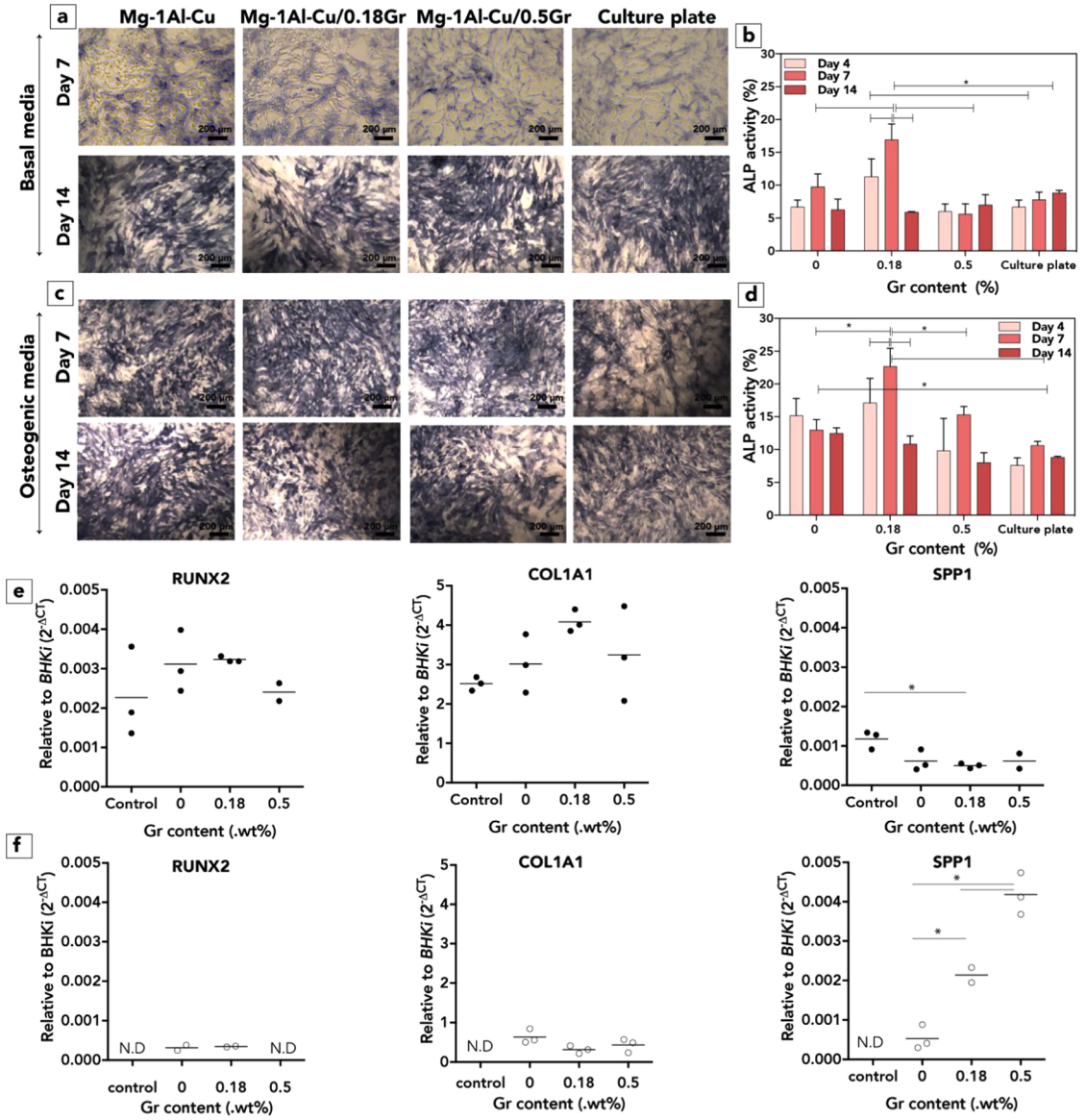

Figure 6. Osteogenic potential of Mg−1Al−Cu/*x*Gr nanocomposite samples. Alkaline phosphatase (ALP) staining images and corresponding quantification in (a, b) basal and (c, d) osteogenic media during 14 days of *in vitro* culture (*$P < 0.05$). Gene expression analysis confirmed the presence of osteogenic markers after (e) 7 days in the osteogenic medium, (f) 14 days in the basal medium with controls cultured in the osteogenic medium.

■ ASSOCIATED CONTENT

Supporting Information

The Supporting Information is available free of charge at https://pubs.acs.org/doi/10.1021/acsbiomaterials.0c00613.

X-ray-diffraction patterns of Mg−1Al−Cu/*x*Gr implants; evaluation of theoretical and experimental density of Mg−1Al−Cu/*x*Gr implants (PDF)

■ AUTHOR INFORMATION

Corresponding Authors

Mahshid Kharaziha − *Department of Materials Engineering, Isfahan University of Technology, Isfahan 84156-83111, Iran*; Email: kharaziha@cc.iut.ac.ir

Miguel Castilho − *Department of Orthopedics, University Medical Center Utrecht, 3584 CX Utrecht, The Netherlands; Regenerative Medicine Utrecht, 3584 CT Utrecht, The Netherlands; Department of Biomedical Engineering, Eindhoven University of Technology, 5612 AZ Eindhoven, The Netherlands*; orcid.org/0000-0002-4269-5889; Email: M.DiasCastilho@umcutrecht.nl

Authors

Narges Safari − *Department of Materials Engineering, Isfahan University of Technology, Isfahan 84156-83111, Iran*

Nasim Golafshan − *Department of Orthopedics, University Medical Center Utrecht, 3584 CX Utrecht, The Netherlands; Regenerative Medicine Utrecht, 3584 CT Utrecht, The Netherlands*

Mohammad Reza Toroghinejad − *Department of Materials Engineering, Isfahan University of Technology, Isfahan 84156-83111, Iran*

Lizette Utomo − *Department of Oral and Maxillofacial Surgery and Special Dental Care, University Medical Center Utrecht, 3584 CX Utrecht, The Netherlands*

https://dx.doi.org/10.1021/acsbiomaterials.0c00613
ACS Biomater. Sci. Eng. 2020, 6, 6253−6262

Jos Malda − *Department of Orthopedics, University Medical Center Utrecht, 3584 CX Utrecht, The Netherlands; Regenerative Medicine Utrecht, 3584 CT Utrecht, The Netherlands; Department of Equine Sciences, Faculty of Veterinary Sciences, Utrecht University, 3584 CS Utrecht, The Netherlands;* orcid.org/0000-0002-9241-7676

Complete contact information is available at: https://pubs.acs.org/10.1021/acsbiomaterials.0c00613

Author Contributions

[▽]N.S. and N.G. shared the authorship.

Notes

The authors declare no competing financial interest.

■ ACKNOWLEDGMENTS

The research leading to these results has received financial support from Isfahan University of Technology. M.C. and J.M. acknowledge the partners of Regenerative Medicine Crossing Borders (www.regmedxb.com) powered by Health ~ Holland, Top Sector Life Sciences & Health, as well as the support of the Dutch Arthritis Foundation (LLP-12 and LLP-22). In addition, the authors are very grateful to Inge Dokter for all of the support with the cell harvesting, in vitro culture, and gene expression analysis.

■ REFERENCES

(1) Castilho, M.; Moseke, C.; Ewald, A.; Gbureck, U.; Groll, J.; Pires, I.; Teßmar, J.; Vorndran, E. Direct 3D powder printing of biphasic calcium phosphate scaffolds for substitution of complex bone defects. *Biofabrication* **2014**, *6*, No. 015006.

(2) Hu, C.; Ashok, D.; Nisbet, D. R.; Gautam, V. Bioinspired surface modification of orthopedic implants for bone tissue engineering. *Biomaterials* **2019**, *219*, No. 119366.

(3) Golafshan, N.; Zaharievski, S.; Brommer, H.; Kadumudi, F. B.; Dolatshahi-Pirouz, A.; Gbureck, U.; Weeren, R.; Castilho, M.; Malda, J.; Vorndran, E. Tough magnesium phosphate-based 3D-printed implants induce bone regeneration in an equine defect model. *Biomaterials* **2020**, *261*, No. 120302.

(4) Sallica-Leva, E.; Caram, R.; Jardini, A.; Fogagnolo, J. Ductility improvement due to martensite α' decomposition in porous Ti−6Al−4V parts produced by selective laser melting for orthopedic implants. *J. Mech. Behav. Biomed. Mater.* **2016**, *54*, 149−158.

(5) Jensen, T.; Jakobsen, T.; Baas, J.; Nygaard, J. V.; Dolatshahi-Pirouz, A.; Hovgaard, M. B.; Foss, M.; Bünger, C.; Besenbacher, F.; Søballe, K. Hydroxyapatite nanoparticles in poly-D, L-lactic acid coatings on porous titanium implants conducts bone formation. *J. Biomed. Mater. Res., Part A* **2010**, *95A*, 665−672.

(6) Majumdar, J. D.; Kumar, A.; Pityana, S.; Manna, I. Laser surface melting of AISI 316L stainless steel for bio-implant application. *Proc. Natl. Acad. Sci., India, Sect. A* **2018**, *88*, 387−403.

(7) Xiang, D.; Wang, P.; Tan, X.; Chandra, S.; Wang, C.; Nai, M.; Tor, S.; Liu, W.; Liu, E. Anisotropic microstructure and mechanical properties of additively manufactured Co−Cr−Mo alloy using selective electron beam melting for orthopedic implants. *Mater. Sci. Eng. A* **2019**, *765*, No. 138270.

(8) Pan, Y.; He, S.; Wang, D.; Huang, D.; Zheng, T.; Wang, S.; Dong, P.; Chen, C. In vitro degradation and electrochemical corrosion evaluations of microarc oxidized pure Mg, Mg−Ca and Mg−Ca−Zn alloys for biomedical applications. *Mater. Sci. Eng., C* **2015**, *47*, 85−96.

(9) Trumbo, P.; Schlicker, S.; Yates, A. A.; Poos, M. Dietary reference intakes for energy, carbohdrate, fiber, fat, fatty acids, cholesterol, protein and amino acids. *J. Acad. Nutr. Diet.* **2002**, *102*, 1621.

(10) Staiger, M. P.; Pietak, A. M.; Huadmai, J.; Dias, G. Magnesium and its alloys as orthopedic biomaterials: a review. *Biomaterials* **2006**, *27*, 1728−1734.

(11) Song, G. L.; Atrens, A. Corrosion mechanisms of magnesium alloys. *Adv. Eng. Mater.* **1999**, *1*, 11−33.

(12) Li, X.; Liu, X.; Wu, S.; Yeung, K.; Zheng, Y.; Chu, P. K. Design of magnesium alloys with controllable degradation for biomedical implants: From bulk to surface. *Acta Biomater.* **2016**, *45*, 2−30.

(13) Zhang, L.-N.; Hou, Z.-T.; Ye, X.; Xu, Z.-B.; Bai, X.-L.; Shang, P. The effect of selected alloying element additions on properties of Mg-based alloy as bioimplants: A literature review. *Front. Mater. Sci.* **2013**, *7*, 227−236.

(14) Ding, Y.; Li, Y.; Lin, J.; Wen, C. Effects of zirconium and strontium on the biocorrosion of Mg−Zr−Sr alloys for biodegradable implant applications. *J. Mater. Chem. B* **2015**, *3*, 3714−3729.

(15) Dambatta, M.; Izman, S.; Yahaya, B.; Lim, J.; Kurniawan, D. Mg-based bulk metallic glasses for biodegradable implant materials: A review on glass forming ability, mechanical properties, and biocompatibility. *J. Non-Cryst. Solids* **2015**, *426*, 110−115.

(16) Safari, N.; Toroghinejad, M. R.; Kharaziha, M. Influence of copper on the structural, mechanical, and biological characteristics of Mg−1Al−Cu alloy. *Mater. Chem. Phys.* **2019**, *237*, No. 121838.

(17) Secinti, K. D.; Özalp, H.; Attar, A.; Sargon, M. F. Nanoparticle silver ion coatings inhibit biofilm formation on titanium implants. *J. Clin. Neurosci.* **2011**, *18*, 391−395.

(18) Mohanty, S.; Alm, M.; Hemmingsen, M.; Dolatshahi-Pirouz, A.; Trifol, J.; Thomsen, P.; Dufva, M.; Wolff, A.; Emnéus, J. 3D printed silicone−hydrogel scaffold with enhanced physicochemical properties. *Biomacromolecules* **2016**, *17*, 1321−1329.

(19) Shuai, C.; Wang, B.; Yang, Y.; Peng, S.; Gao, C. 3D honeycomb nanostructure-encapsulated magnesium alloys with superior corrosion resistance and mechanical properties. *Composites, Part B* **2019**, *162*, 611−620.

(20) Sadeghinezhad, E.; Mehrali, M.; Akhiani, A. R.; Latibari, S. T.; Dolatshahi-Pirouz, A.; Metselaar, H. S. C.; Mehrali, M. Experimental study on heat transfer augmentation of graphene based ferrofluids in presence of magnetic field. *Appl. Therm. Eng.* **2017**, *114*, 415−427.

(21) Yang, M.; Weng, L.; Zhu, H.; Fan, T.; Zhang, D. Simultaneously enhancing the strength, ductility and conductivity of copper matrix composites with graphene nanoribbons. *Carbon* **2017**, *118*, 250−260.

(22) Kumar, P.; Huo, P.; Zhang, R.; Liu, B. Antibacterial properties of graphene-based nanomaterials. *Nanomaterials* **2019**, *9*, 737.

(23) Qiu, J.; Guo, J.; Geng, H.; Qian, W.; Liu, X. Three-dimensional porous graphene nanosheets synthesized on the titanium surface for osteogenic differentiation of rat bone mesenchymal stem cells. *Carbon* **2017**, *125*, 227−235.

(24) Chen, Y.; Guo, Y.; Gupta, M.; Shim, V. Dynamic tensile response of magnesium nanocomposites and the effect of nano-particles. *Mater. Sci. Eng. A* **2013**, *582*, 359−367.

(25) Busk, R. S. *Magnesium and Its Alloys*; John Wiley and Sons: New York, 2007; Vol. *8*, pp 259−265.

(26) Kubota, M.; Wynne, B. Electron backscattering diffraction analysis of mechanically milled and spark plasma sintered pure aluminium. *Scr. Mater.* **2007**, *57*, 719−722.

(27) Cai, B.; Kong, Q.; Lu, L.; Lu, K. Interface controlled diffusional creep of nanocrystalline pure copper. *Scr. Mater.* **1999**, *41*, 755−759.

(28) Gupta, M.; Wong, W. Magnesium-based nanocomposites: Lightweight materials of the future. *Mater. Charact.* **2015**, *105*, 30−46.

(29) Zhang, S.; Zhang, X.; Zhao, C.; Li, J.; Song, Y.; Xie, C.; Tao, H.; Zhang, Y.; He, Y.; Jiang, Y. Research on an Mg−Zn alloy as a degradable biomaterial. *Acta Biomater.* **2010**, *6*, 626−640.

(30) GUMARGALIEVA, K.; ZAIKOV, G. BURN DRESSINGS SORPTION AND DESORPTION KINETICS AND MECHANISM. *Key Eng. Mater., Vol. II: Interdiscip. Concepts Res.* **2014**, *2*, 257.

(31) Pfaffl, M. W.; Tichopad, A.; Prgomet, C.; Neuvians, T. P. Determination of stable housekeeping genes, differentially regulated target genes and sample integrity: BestKeeper−Excel-based tool using pair-wise correlations. *Biotechnol. Lett.* **2004**, *26*, 509−515.

(32) Utomo, L.; Bastiaansen-Jenniskens, Y. M.; Verhaar, J. A.; van Osch, G. J. Cartilage inflammation and degeneration is enhanced by pro-inflammatory (M1) macrophages in vitro, but not inhibited directly by anti-inflammatory (M2) macrophages. *Osteoarthritis Cartilage* **2016**, *24*, 2162−2170.
(33) Utomo, L.; Pleumeekers, M. M.; Nimeskern, L.; Nürnberger, S.; Stok, K. S.; Hildner, F.; van Osch, G. J. Preparation and characterization of a decellularized cartilage scaffold for ear cartilage reconstruction. *Biomed. Mater.* **2015**, *10*, No. 015010.
(34) Longoni, A.; Utomo, L.; Van Hooijdonk, I.; Bittermann, G.; Vetter, V.; Spanjer, E. K.; Ross, J.; Rosenberg, A.; Gawlitta, D. The chondrogenic differentiation potential of dental pulp stem cells. *Eur. Cells Mater.* **2020**, *39*, 121−135.
(35) Klotz, B. J.; Oosterhoff, L. A.; Utomo, L.; Lim, K. S.; Vallmajo-Martin, Q.; Clevers, H.; Woodfield, T. B.; Rosenberg, A. J.; Malda, J.; Ehrbar, M.; et al. A versatile biosynthetic hydrogel platform for engineering of tissue analogues. *Adv. Healthcare Mater.* **2019**, *8*, No. 1900979.
(36) Yazdani, B.; Xia, Y.; Ahmad, I.; Zhu, Y. Graphene and carbon nanotube (GNT)-reinforced alumina nanocomposites. *J. Eur. Ceram. Soc.* **2015**, *35*, 179−186.
(37) Ptak, M.; Kaczyński, P.; Wilhelm, J.; Margarido, J. M.; Marques, P. A.; Pinto, S. C.; Alves de Sousa, R. J.; Fernandes, F. A. Graphene-enriched agglomerated cork material and its behaviour under quasi-static and dynamic loading. *Materials* **2019**, *12*, No. 151.
(38) Jiang, X.; Liu, W.; Li, Y.; Shao, Z.; Luo, Z.; Zhu, D.; Zhu, M. Microstructures and mechanical properties of Cu/Ti3SiC2/C/graphene nanocomposites prepared by vacuum hot-pressing sintering and hot isostatic pressing. *Composites, Part B* **2018**, *141*, 203−213.
(39) Das, A.; Harimkar, S. P. Effect of graphene nanoplate and silicon carbide nanoparticle reinforcement on mechanical and tribological properties of spark plasma sintered magnesium matrix composites. *J. Mater. Sci. Technol.* **2014**, *30*, 1059−1070.
(40) Chen, S.; Brown, L.; Levendorf, M.; Cai, W.; Ju, S.-Y.; Edgeworth, J.; Li, X.; Magnuson, C. W.; Velamakanni, A.; Piner, R. D.; et al. Oxidation resistance of graphene-coated Cu and Cu/Ni alloy. *ACS Nano* **2011**, *5*, 1321−1327.
(41) Munir, K.; Wen, C.; Li, Y. Graphene nanoplatelets-reinforced magnesium metal matrix nanocomposites with superior mechanical and corrosion performance for biomedical applications. *J. Magnesium Alloys* **2020**, *8*, 269−290.
(42) Böhm, S. Graphene against corrosion. *Nat. Nanotechnol.* **2014**, *9*, 741−742.
(43) Li, H.; Xie, X.; Zhao, K.; Wang, Y.; Zheng, Y.; Wang, W.; Qin, L. In vitro and in vivo studies on biodegradable CaMgZnSrYb high-entropy bulk metallic glass. *Acta Biomater.* **2013**, *9*, 8561−8573.
(44) Zhang, S.; Li, J.; Song, Y.; Zhao, C.; Zhang, X.; Xie, C.; Zhang, Y.; Tao, H.; He, Y.; Jiang, Y.; Bian, Y. In vitro degradation, hemolysis and MC3T3-E1 cell adhesion of biodegradable Mg−Zn alloy. *Mater. Sci. Eng., C* **2009**, *29*, 1907−1912.
(45) Rajapaksha, P.; Cheeseman, S.; Hombsch, S.; Murdoch, B. J.; Gangadoo, S.; Blanch, E. W.; Truong, Y.; Cozzolino, D.; McConville, C. F.; Crawford, R. J.; et al. Antibacterial Properties of Graphene Oxide−Copper Oxide Nanoparticle Nanocomposites. *ACS Appl. Bio Mater.* **2019**, *2*, 5687−5696.
(46) Liu, S.; Zeng, T. H.; Hofmann, M.; Burcombe, E.; Wei, J.; Jiang, R.; Kong, J.; Chen, Y. Antibacterial activity of graphite, graphite oxide, graphene oxide, and reduced graphene oxide: membrane and oxidative stress. *ACS Nano* **2011**, *5*, 6971−6980.
(47) Akhavan, O.; Ghaderi, E. Toxicity of graphene and graphene oxide nanowalls against bacteria. *ACS Nano* **2010**, *4*, 5731−5736.
(48) Veerapandian, M.; Zhang, L.; Krishnamoorthy, K.; Yun, K. Surface activation of graphene oxide nanosheets by ultraviolet irradiation for highly efficient anti-bacterials. *Nanotechnology* **2013**, *24*, No. 395706.
(49) Kiani, F.; Astani, N. A.; Rahighi, R.; Tayyebi, A.; Tayebi, M.; Khezri, J.; Hashemi, E.; Rothlisberger, U.; Simchi, A. Effect of graphene oxide nanosheets on visible light-assisted antibacterial activity of vertically-aligned copper oxide nanowire arrays. *J. Colloid Interface Sci.* **2018**, *521*, 119−131.
(50) Zhang, Q.; Li, K.; Yan, J.; Wang, Z.; Wu, Q.; Bi, L.; Yang, M.; Han, Y. Graphene coating on the surface of CoCrMo alloy enhances the adhesion and proliferation of bone marrow mesenchymal stem cells. *Biochem. Biophys. Res. Commun.* **2018**, *497*, 1011−1017.
(51) Liu, C.; Fu, X.; Pan, H.; Wan, P.; Wang, L.; Tan, L.; Wang, K.; Zhao, Y.; Yang, K.; Chu, P. K. Biodegradable Mg-Cu alloys with enhanced osteogenesis, angiogenesis, and long-lasting antibacterial effects. *Sci. Rep.* **2016**, *6*, No. 27374.
(52) Li, N.; Zheng, Y. Novel magnesium alloys developed for biomedical application: a review. *J. Mater. Sci. Technol.* **2013**, *29*, 489−502.
(53) Qiu, Z.; Wang, R.; Wu, J.; Zhang, Y.; Qu, Y.; Wu, X. Graphene oxide as a corrosion-inhibitive coating on magnesium alloys. *RSC Adv.* **2015**, *5*, 44149−44159.
(54) Ku, S. H.; Lee, M.; Park, C. B. Carbon-based nanomaterials for tissue engineering. *Adv. Healthcare Mater.* **2013**, *2*, 244−260.
(55) Yan, X.; Yang, W.; Shao, Z.; Yang, S.; Liu, X. Graphene/single-walled carbon nanotube hybrids promoting osteogenic differentiation of mesenchymal stem cells by activating p38 signaling pathway. *Int. J. Nanomed.* **2016**, *11*, 5473.
(56) Zhang, Y.; Ali, S. F.; Dervishi, E.; Xu, Y.; Li, Z.; Casciano, D.; Biris, A. S. Cytotoxicity effects of graphene and single-wall carbon nanotubes in neural phaeochromocytoma-derived PC12 cells. *ACS Nano* **2010**, *4*, 3181−3186.
(57) Chang, Y.; Yang, S.-T.; Liu, J.-H.; Dong, E.; Wang, Y.; Cao, A.; Liu, Y.; Wang, H. In vitro toxicity evaluation of graphene oxide on A549 cells. *Toxicol. Lett.* **2011**, *200*, 201−210.

https://dx.doi.org/10.1021/acsbiomaterials.0c00613
ACS Biomater. Sci. Eng. 2020, 6, 6253−6262